Supplementary material

Model carbon materials derived from tannin to assess the importance of pore connectivity in supercapacitors

Jimena Castro-Gutiérrez,[a] Noel Díez,[b] Marta Sevilla,[b] María Teresa Izquierdo,[c] Alain Celzard [a] and Vanessa Fierro *[a]

[a] Université de Lorraine, Institut Jean Lamour, UMR CNRS 7198, 27 Rue Philippe Séguin, 88051 Epinal Cedex 9, France.
[b] Instituto de Ciencia y Tecnología del Carbono (INCAR-CSIC), Francisco Pintado Fe 26, 33011 Oviedo, Spain.
[c] Instituto de Carboquímica (ICB-CSIC), Miguel Luesma Castán 4, E-50018 Zaragoza, Spain.

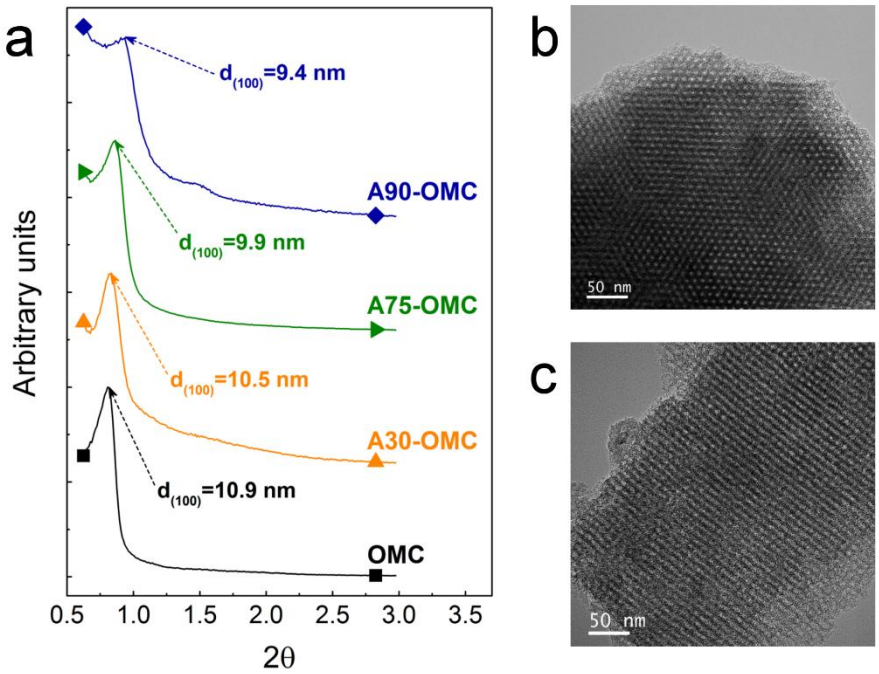

Figure S1. (a) Small-angle XRD measurements for the OMC and for AOMCs activated during 30, 75 and 90 min [Adapted with permission from Castro-Gutiérrez et al. *ACS Sustainable Chem. Eng.* 2019, 7, 17627−17635, 2019. Copyright 2019 American Chemical Society]. (b, c) TEM images of A90-OMC with a BO of 78 %.

Table S1. Pore texture parameters of the two series of activated materials derived from disordered and ordered mesoporous carbons, DMC and OMC, respectively.

Sample	Act. Time [min]	S_{NLDFT} [$m^2 g^{-1}$]	A_{BET} [$m^2 g^{-1}$]	V_{tot} [$cm^3 g^{-1}$]	$V_{u\mu}$ [$cm^3 g^{-1}$]	$V_{s\mu}$ [$cm^3 g^{-1}$]	V_{meso} [$cm^3 g^{-1}$]
DMC	0	732	533	0.41	0.16	0.03	0.22
A15-DMC	15	1175	995	0.64	0.23	0.13	0.28
A30-DMC	30	1430	1436	0.89	0.20	0.30	0.39
A45-DMC	**45**	**1578**	**1819**	**1.09**	**0.15**	**0.47**	**0.46**
A60-DMC	60	1566	1991	1.19	0.12	0.53	0.54
OMC	0	761	567	0.36	0.16	0.04	0.16
A15-OMC	15	1085	894	0.54	0.21	0.10	0.23
A30-OMC	30	1333	1222	0.71	0.22	0.20	0.29
A45-OMC	45	1416	1387	0.80	0.22	0.26	0.33
A60-OMC	60	1480	1479	0.86	0.20	0.30	0.35
A75-OMC	**75**	**1614**	**1867**	**1.11**	**0.14**	**0.48**	**0.49**
A90-OMC	90	1576	1999	1.23	0.09	0.54	0.60
A105-OMC	105	1644	2061	1.19	0.12	0.55	0.53
A120-OMC	120	1215	1642	0.95	0.06	0.42	0.47

S_{NLDFT} and A_{BET}, specific surface areas calculated by applying 2D-NLDFT HS and BET models, respectively. Parameters calculated from the 2D-NLDFT HS PSD: V_{tot}, total pore volume; $V_{u\mu}$, ultramicropore volume (w < 0.7 nm); $V_{s\mu}$, supermicropore volume (0.7 < w < 2 nm); $V_{meso} = V_{tot} - V_{s\mu} - V_{u\mu}$, mesopore volume (2 nm < w).

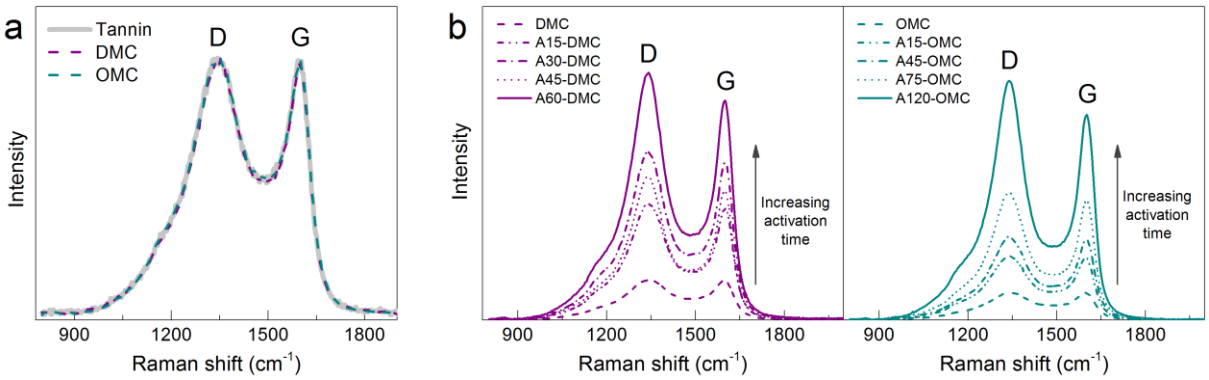

Figure S2. 1st order Raman spectra of (a) as-synthesized DMC, OMC and mimosa tannin carbonized at the same temperature of 900°C, and (b) of A*t*-DMC and A*t*-OMC series of materials.

Supplementary note. On the shape analysis of the secondary desorption branches of A*t*-DMC materials

A first initial visual inspection of the secondary desorption branches in both ranges ($p/p_0 < 0.6$ and $p/p_0 > 0.6$) was carried out, see Figure S3a,c showing the example for sample A15-DMC. Afterwards, the different sections of the secondary desorption branches were normalized (between 0 and 1) in both axes and plotted together as shown in Figure S3b,d. After normalization, a marked difference between the secondary branches of the upper section of the hysteresis loop ($p/p_0 > 0.6$, Figure S3d) can be observed, while those of the lower part ($p/p_0 < 0.6$, Figure S3b) practically overlap, *i.e.*, they have the same shape. The same behavior was observed for the rest of the disordered samples. The calculation of the slopes of the desorption branches (results presented in the main text) was carried out with the aim of further analyzing the behavior of the secondary branches, quantifying small or large differences between them and evaluating the presence of pores with open and restricted access.

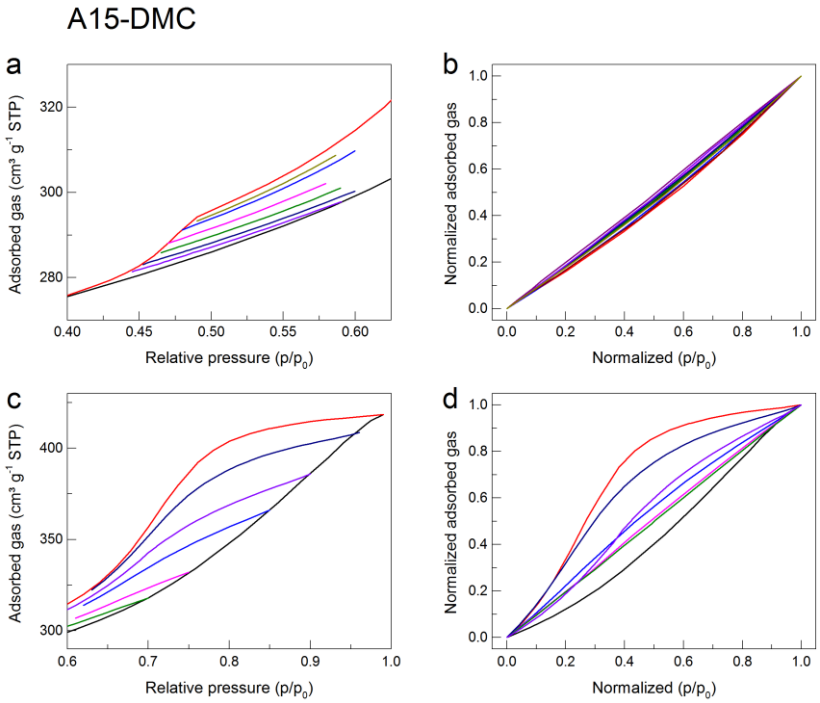

Figure S3. Different sections of the secondary desorption branches in (a) $p/p_0 < 0.6$ and (c) $p/p_0 > 0.6$ ranges for A15-DMC sample. The normalized sections for (b) low- and (d) high-relative pressure regions ($p/p_0 < 0.6$ and $p/p_0 > 0.6$, respectively) are also shown.

Table S2. Elemental analysis of the At-DMC and At-OMC series of materials. The values shown are the averages of two different measurements. The difference between the measured O content (O^{meas}) and that calculated by difference (O^{dif}) is due to the ash content; as expected, the difference between O^{dif} and O^{meas} increases with activation time as the ash content becomes more important with respect to the remaining carbon material.

Sample	C (wt %)	H (wt %)	N (wt %)	S (wt %)	O^{dif} (wt %)	O^{meas} (wt %)
DMC	90.5	0.7	0.3	0.0	8.5	10.0
A15-DMC	90.2	0.5	0.4	0.0	8.9	7.8
A30-DMC	88.1	0.5	0.4	0.0	11	8.7
A45-DMC	85	0.6	0.6	0.0	13.8	9.5
A60-DMC	78.3	0.5	1.1	0.0	20.1	10.6
OMC	91.5	0.7	0.5	0.0	7.3	5.2
A30-OMC	90.9	0.7	0.4	0.0	8	4.4
A45-OMC	89.0	0.7	0.4	0.0	9.9	4.8
A60-OMC	88.9	0.6	0.4	0.0	10.1	4.6
A75-OMC	87.9	0.6	0.6	0.0	10.9	5.1
A90-OMC	75.3	0.6	0.7	0.0	23.4	6.2
A105-OMC	82.9	0.5	0.7	0.0	15.9	6.2
A120-OMC	51.1	0.3	0.8	0.0	47.8	6.2

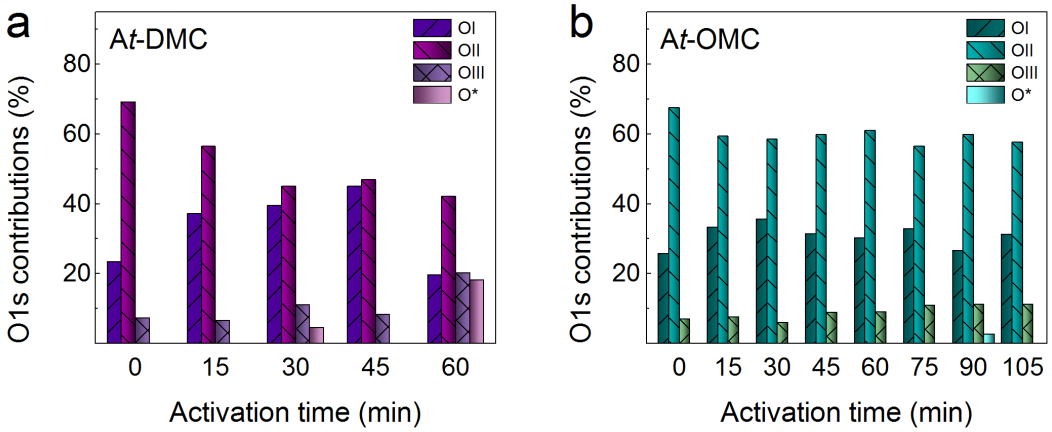

Figure S4. O1s contributions to the different functional groups for the (a) A*t*-DMC and (d) A*t*-OMC series.

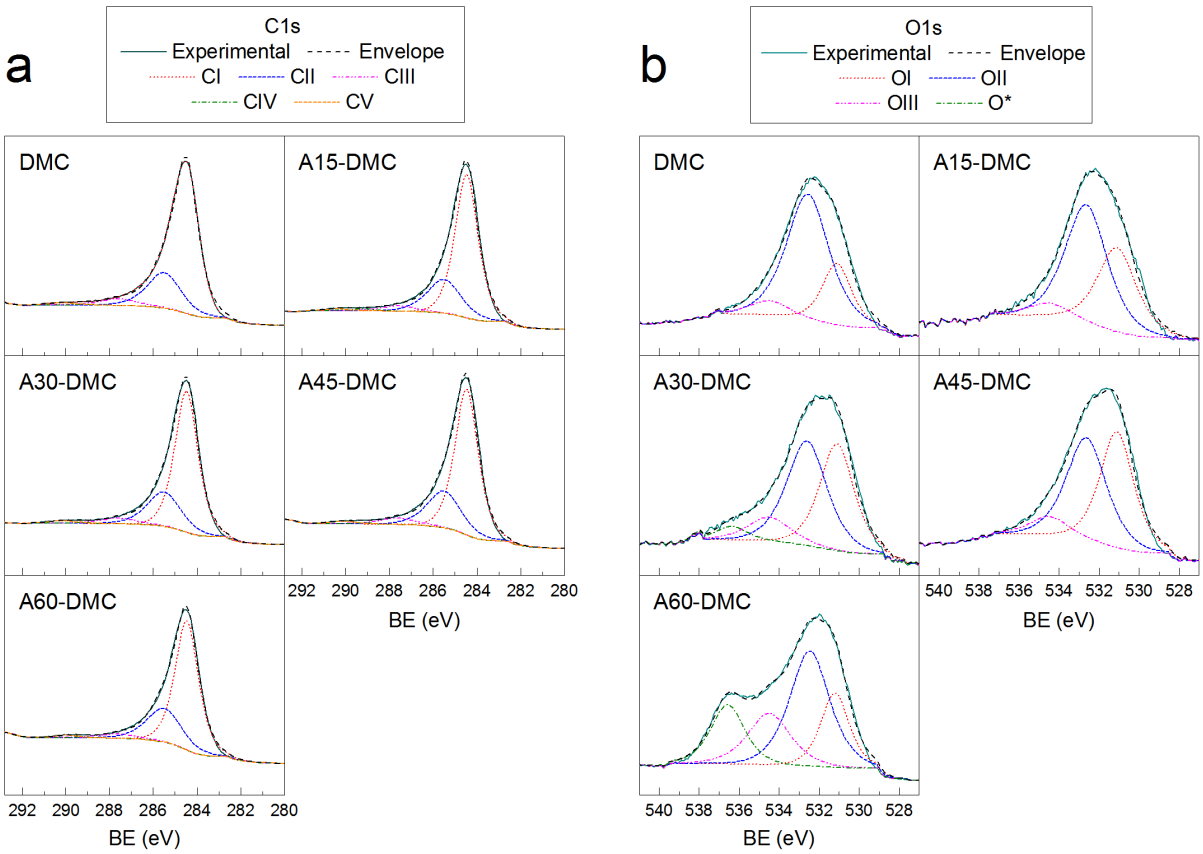

Figure S5. (a) C1s and (b) O1s peaks obtained by XPS analysis of A*t*-DMC materials.

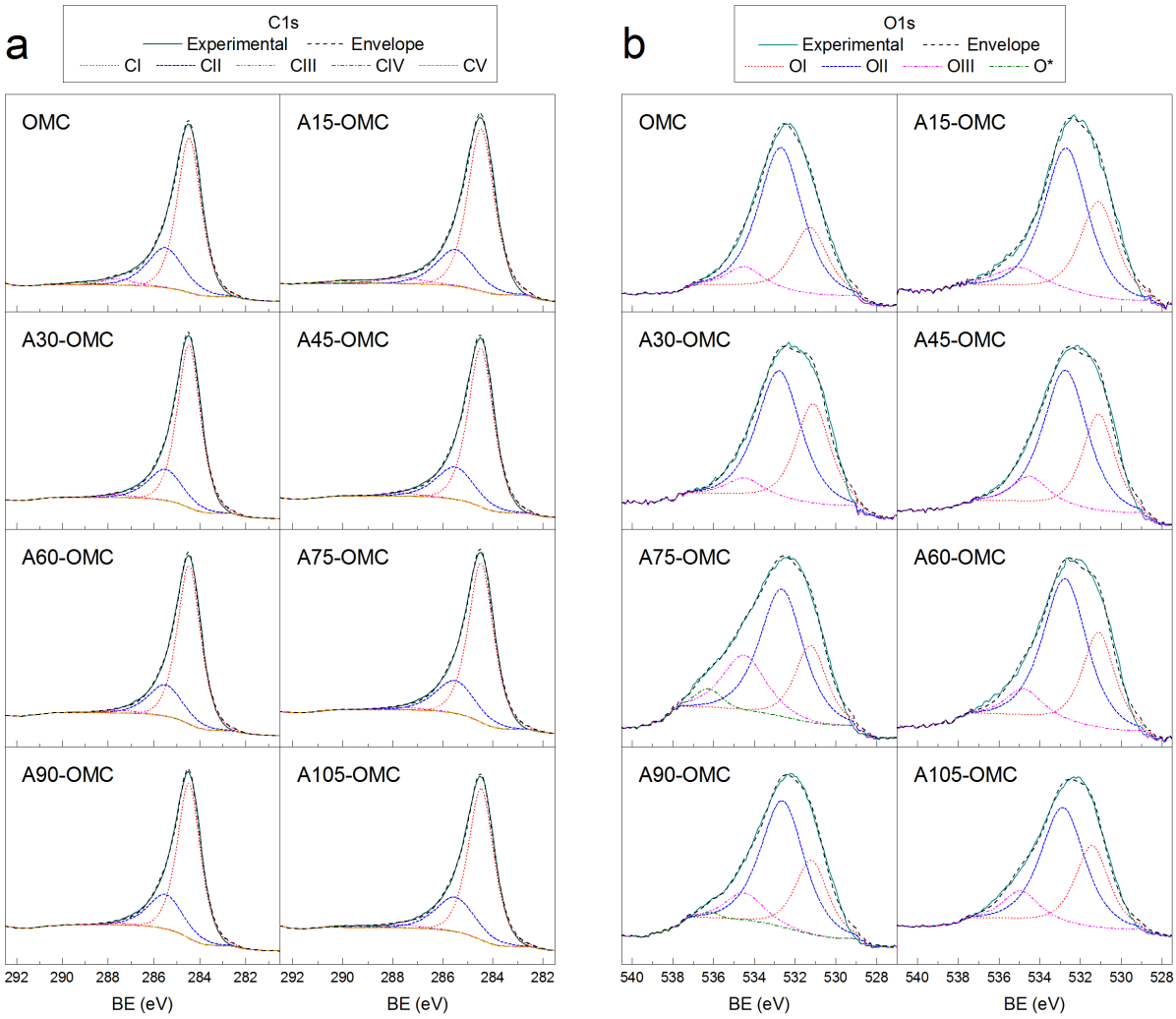

Figure S6. (a) C1s and (b) O1s peaks obtained by XPS analysis of A*t*-OMC materials.

Table S3. Peak assignment and relative contributions of surface functionalities obtained by XPS of the two series of activated materials derived from disordered (DMC) and ordered (OMC) mesoporous carbons.

	C1s contributions					O1s contributions			
Sample	**CI A (BE) [% (eV)]**	**CII A (BE) [% (eV)]**	**CIII A (BE) [% (eV)]**	**CIV A (BE) [% (eV)]**	**CV A (BE) [% (eV)]**	**OI A (BE) [% (eV)]**	**OII A (BE) [% (eV)]**	**OIII A (BE) [% (eV)]**	**O* A (BE) [% (eV)]**
DMC	68.4 (284.5)	24.8 (285.5)	5.3 (287.6)	0.3 (289.1)	1.2 (290.1)	23.4 (531.1)	69.2 (532.6)	7.3 (534.5)	--
A15-DMC	69.7 (284.4)	24.2 (285.5)	3.9 (287.6)	1.1 (289.2)	1.0 (290.4)	37.1 (531.1)	56.4 (532.3)	6.5 (534.5)	--
A30-DMC	69.0 (284.5)	24.6 (285.5)	4.5 (287.6)	0.3 (289.2)	1.6 (290.1)	39.5 (531.1)	45.0 (532.6)	11.0 (534.5)	4.5 (536.4)
A45-DMC	**68.4 (284.5)**	**25.1 (285.5)**	**4.8 (287.6)**	**0.4 (289.2)**	**1.3 (290.2)**	**45.0 (531.1)**	**46.8 (532.6)**	**8.2 (534.5)**	**--**
A60-DMC	68.4 (284.4)	26.3 (285.5)	3.7 (287.6)	0.3 (289.2)	1.3 (290.0)	19.6 (531.2)	42.1 (532.5)	20.1 (534.5)	18.2 (536.6)
OMC	68.3 (284.4)	26.9 (285.5)	3.6 (287.6)	1.2 (289.2)	--	25.6 (531.3)	67.4 (532.7)	7.0 (534.5)	
A30-OMC	76.3 (284.5)	21.8 (285.5)	1.9 (287.6)	--	--	35.6 (531.1)	58.4 (532.8)	5.9 (534.5)	
A45-OMC	75.1 (284.5)	22.9 (285.5)	2.0 (287.6)	--	--	31.3 (531.1)	59.7 (532.7)	8.9 (534.5)	
A60-OMC	75.7 (284.5)	22.2 (285.5)	2.1 (287.6)	--	--	30.1 (531.1)	60.9 (532.7)	9.0 (534.5)	
A75-OMC	**74.6 (284.5)**	**23.5 (285.5)**	**1.9 (287.6)**	**--**	**--**	**32.8 (531.1)**	**56.4 (532.7)**	**10.9 (534.5)**	
A90-OMC	73.9 (284.5)	24.7 (285.5)	1.4 (287.6)	--	--	26.6 (531.2)	59.7 (532.6)	11.1 (534.5)	2.6 (536.2)
A105-OMC	71.5 (284.5)	25.1 (285.5)	2.1 (287.6)	1.4 (289.2)	--	31.2 (531.4)	57.6 (532.8)	11.2 (534.9)	

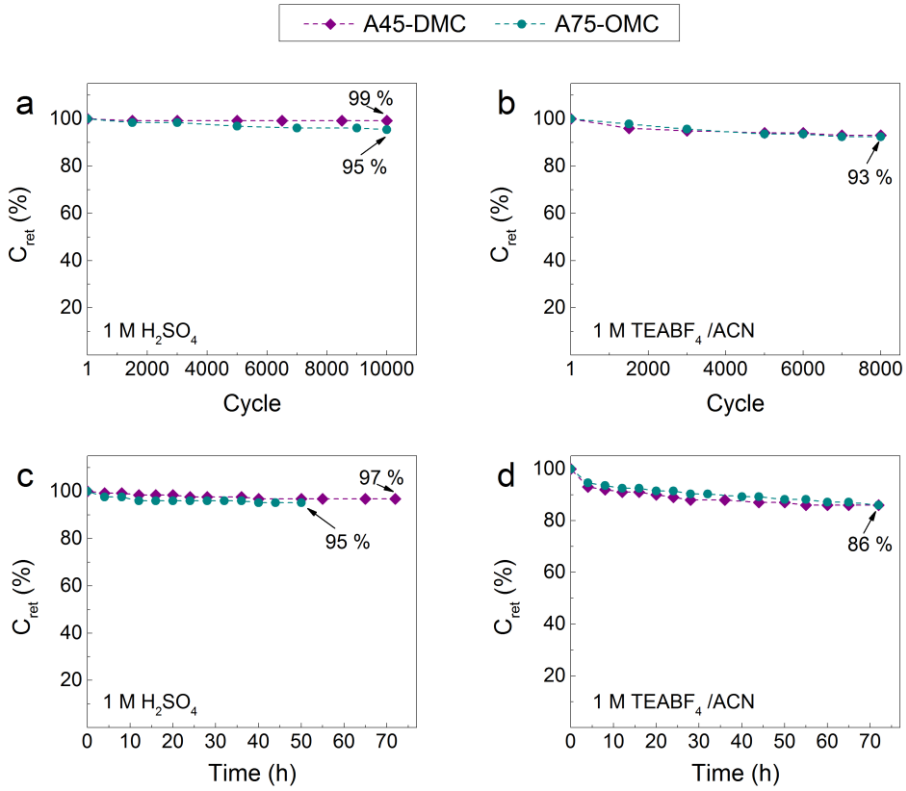

Figure S7. Long-term stability of A45-DMC and A75-OMC in aqueous (1 M H_2SO_4) and organic (1 M $TEABF_4$/ACN) electrolytes after (a, b) continuous cycling at 5 A g^{-1} and (c, d) potentiostatic hold at the maximum potential (1 V and 2.7 V for aqueous and organic electrolytes, respectively).

Table S4. BET area and electrochemical performance in aqueous (H_2SO_4) and organic electrolytes ($TEABF_4$) of this study and others reported in the literature. Names of the samples correspond to those of their source and reference numbers are those used in the main article.

Sample	Commentary	A_{BET} ($m^2 g^{-1}$)	Cell type	Aqueous electrolyte (H_2SO_4)		Organic electrolyte ($TEABF_4$)		Ref
				C_e	C_{ret}	C_e	C_{ret}	
A45-DMC A75-OMC	Soft-templated by mechanosynthesis, CO_2-activated mesoporous carbons from mimosa tannin	1819 1867	2e	148 Fg^{-1} at 0.2 Ag^{-1} 148 Fg^{-1} at 0.2 Ag^{-1}	58 % at 80 Ag^{-1} 70 % at 80 Ag^{-1}	114 Fg^{-1} at 0.2 Ag^{-1} 108 Fg^{-1} at 0.2 Ag^{-1}	56 % at 40 Ag^{-1} 41 % at 40 Ag^{-1}	This study [30]
CK-800 CK-900	Salt templated-assisted K_2CO_3-activated tannic acid	2510 2740	2e	260 Fg^{-1} at 0.2 Ag^{-1} 210 Fg^{-1} at 0.2 Ag^{-1}	45 % at 80 Ag^{-1} 46 % at 80 Ag^{-1}	140 Fg^{-1} at 0.2 Ag^{-1} 160 Fg^{-1} at 0.2 Ag^{-1}	69 % at 20 Ag^{-1} 88 % at 20 Ag^{-1}	[20]
PhC GaC CatC TanC	Hard templated (SBA-15) OMCs from phloroglucinol, galic acid, catechin and mimosa tannin	1094 1045 917 1006	3e	196 ± 12 Fg^{-1} at 0.2 Ag^{-1}	66 % at 24 Ag^{-1} 61 % at 24 Ag^{-1} 48 % at 24 Ag^{-1} 51 % at 24 Ag^{-1}			[23]
Gyroid Cylinder	Soft-templated by EISA, KOH-activated mesoporous carbons	93	2e			155 Fg^{-1} at 0.05 Ag^{-1} 135 Fg^{-1} at 0.05 Ag^{-1}	93 % at 5 Ag^{-1}	[31]
C3/30	Soft templated by phase separation, CO_2-activated OMC from mimosa tannin	1152	2e	244 Fg^{-1} at 0.2 Ag^{-1}	50 % at 24 Ag^{-1}			[50]
AOW	KOH-activated olive mill wastewater	1952	2e	107 Fg^{-1} at 0.125 Ag^{-1}	66 % at 10 Ag^{-1}			[51]
AC-KOH CESM-300	KOH-activated carbonized chicken eggshell	1575 221	3e	200 Fg^{-1} at 0.2 Ag^{-1} 284 Fg^{-1} at 0.2 Ag^{-1}	63 % at 10 Ag^{-1} 60 % at 10 Ag^{-1}			[52]
ACM-A ACM-B	KOH-activated carbon from ethylene-tar	2652 1107	2e	334 Fg^{-1} at 0.05 Ag^{-1} 183 Fg^{-1} at 0.05 Ag^{-1}	60 % at 5 Ag^{-1} 55 % at 5 Ag^{-1}			[53]
MC-1	Hard templated (foam-like structure) mesoporous carbon spheres from phenol	1321	3e	208 Fg^{-1} at 0.5 Ag^{-1}	70 % at 30 Ag^{-1}	97 Fg^{-1} at 0.5 Ag^{-1}	70 % at 15 Ag^{-1}	[54]
C-1 C-2	Hard templated (SBA-16) OMCs from furfuryl alcohol	1880 1510	2e	172 Fg^{-1} at 0.2 Ag^{-1} 154 Fg^{-1} at 0.2 Ag^{-1}	83 % at 1 Ag^{-1} 86 % at 1 Ag^{-1}	96 Fg^{-1} at 0.2 Ag^{-1} 89 Fg^{-1} at 0.2 Ag^{-1}	90 % at 1 Ag^{-1} 90 % at 1 Ag^{-1}	[55]
L-β-900 L-Y-900	Hard templated (zeolites) OMCs from lignin	785 650	3e	149 Fg^{-1} at 0.05 Ag^{-1} 189 Fg^{-1} at 0.05 Ag^{-1}	66 % at 5 Ag^{-1} 58 % at 5 Ag^{-1}			[56]
CC	Hard templated (solid core, mesoporous shell) carbon spheres	1660	2e	200 Fg^{-1} at 0.1 Ag^{-1}	61 % at 80 Ag^{-1}			[57]
HG180-KB6 HG240-KB6 HG180-KOH	$KHCO_3$- and KOH-activated hydrochars from α-D-glucose	2210 2230 2760	2e	239 Fg^{-1} at 0.1 Ag^{-1} 246 Fg^{-1} at 0.1 Ag^{-1} 270 Fg^{-1} at 0.1 Ag^{-1}	46 % at 90 Ag^{-1} 54 % at 90 Ag^{-1} 51 % at 90 Ag^{-1}			[58]
N0 N1 N2 N3 N4	KOH-activated commercial activated carbon Norit® SX2 POCH-Poland	835 1901 2400 2522 2800	2e	106 Fg^{-1} at 0.05 Ag^{-1} 172 Fg^{-1} at 0.05 Ag^{-1} 182 Fg^{-1} at 0.05 Ag^{-1} 153 Fg^{-1} at 0.05 Ag^{-1} 196 Fg^{-1} at 0.05 Ag^{-1}	46 % at 20 Ag^{-1} 55 % at 20 Ag^{-1} 56 % at 20 Ag^{-1} 90 % at 2 Ag^{-1} ---	46 Fg^{-1} at 0.05 Ag^{-1} 125 Fg^{-1} at 0.05 Ag^{-1} 140 Fg^{-1} at 0.05 Ag^{-1} 120 Fg^{-1} at 0.05 Ag^{-1} 145 Fg^{-1} at 0.05 Ag^{-1}	46 % at 20 Ag^{-1} 82 % at 10 Ag^{-1} --- 66 % at 20 Ag^{-1} 71 % at 20 Ag^{-1}	[59]

Table S5. BET area and electrochemical performance in organic electrolytes ($TEABF_4$) of porous carbon materials reported in the literature. Names of the samples correspond to those of their source and reference numbers are those used in the main article.

Sample	Commentary	A_{BET} ($m^2 g^{-1}$)	Cell type	Organic electrolyte ($TEABF_4$)		Ref
				C_e	C_{ret}	
SWNT solid	Single-walled carbon nanotubes produced by CVD of C_2H_4	1000	2e	80 Fg^{-1} at 0.05 Ag^{-1}	59 % at 10 Ag^{-1}	[60]
Aerosol carbon	Hard templated (silicate) mesoporous particles produced by an aerosol process	1522	2e	115 Fg^{-1} at 0.1 Ag^{-1}	83 % at 10 Ag^{-1}	[61]
CGC-3.5 CGC-5	$ZnCl_2$-activated coffee grounds	940 1021	2e	134 Fg^{-1} at 0.05 Ag^{-1}	30 % at 15 Ag^{-1} 75 % at 20 Ag^{-1}	[62]
NPV1 NPV2 NPV3 NPV4	NaOH-activated carbons from PVDC	1829 2527 2630 2675	2e	108 Fg^{-1} at 0.05 Ag^{-1} 142 Fg^{-1} at 0.05 Ag^{-1} 147 Fg^{-1} at 0.05 Ag^{-1} 155 Fg^{-1} at 0.05 Ag^{-1}	7 % at 16.2 Ag^{-1} 20 % at 15.5 Ag^{-1} 58 % at 17 Ag^{-1} 71 % at 18 Ag^{-1}	[63]
CK-800 CK-850 CK-900	Carbonized potassium citrate	1940 2220 2160	2e	135 Fg^{-1} at 0.05 Ag^{-1} 140 Fg^{-1} at 0.05 Ag^{-1} 125 Fg^{-1} at 0.05 Ag^{-1}	93 % at 40 Ag^{-1} 89 % at 40 Ag^{-1} 92 % at 40 Ag^{-1}	[64]
CMC650 PMC450 MC-2 GC-2	KOH-activated carbons from pine cones, coffee grounds and graphene oxide. Also, carbonized MOFs.	2656 1810 2550 2780	2e	230 Fg^{-1} at 0.5 Ag^{-1} 200 Fg^{-1} at 0.5 Ag^{-1} 167 Fg^{-1} at 1 Ag^{-1} 141 Fg^{-1} at 1 Ag^{-1}	68 % at 10 Ag^{-1} 67 % at 10 Ag^{-1} 87 % at 10 Ag^{-1} 87 % at 10 Ag^{-1}	[65]
PF16G-HA PVA20G-HA LI24G-HA SU24G-HA CE24G-HA	KOH-activated carbons from hydrothermal treatment of graphene oxide mixed with either phenol-formaldehyde, polyvinyl alcohol, lignin, sucrose or cellulose	3523 3192 3026 3355 3117	2e	202 Fg^{-1} at 1 Ag^{-1} 174 Fg^{-1} at 1 Ag^{-1} 190 Fg^{-1} at 1 Ag^{-1} 191 Fg^{-1} at 1 Ag^{-1} 185 Fg^{-1} at 1 Ag^{-1}	86 % at 10 Ag^{-1} 90 % at 10 Ag^{-1} 84 % at 10 Ag^{-1} 90 % at 10 Ag^{-1} 86 % at 10 Ag^{-1}	[66]
a-MEGO	KOH-activated microwave-exfoliated graphene oxide	3100	2e	150 Fg^{-1} at 0.8 Ag^{-1}	92 % at 3.8 Ag^{-1}	[67]
AC-C700 AC-C800 AC-S700 AC-W700 AC-W800	KOH-activated hydrochars from cellulose, potato starch and eucalyptus wood sawdust	2457 2125 2273 2331 2967	2e	185 Fg^{-1} at 0.2 Ag^{-1} 145 Fg^{-1} at 0.2 Ag^{-1} 180 Fg^{-1} at 0.2 Ag^{-1} 190 Fg^{-1} at 0.2 Ag^{-1} 230 Fg^{-1} at 0.2 Ag^{-1}	61 % at 20 Ag^{-1} 79 % at 20 Ag^{-1} 59 % at 20 Ag^{-1} 76 % at 20 Ag^{-1} 81 % at 20 Ag^{-1}	[68]

References (numbers correspond to those used in the main article):

[20] N. Díez, G.A. Ferrero, M. Sevilla, A.B. Fuertes, A sustainable approach to hierarchically porous carbons from tannic acid and their utilization in supercapacitive energy storage systems, J. Mater. Chem. A. 7 (2019) 14280–14290. https://doi.org/10.1039/C9TA01712G.

[23] A. Sanchez-Sanchez, M.T. Izquierdo, J. Ghanbaja, G. Medjahdi, S. Mathieu, A. Celzard, V. Fierro, Excellent electrochemical performances of nanocast ordered mesoporous carbons based on tannin-related polyphenols as supercapacitor electrodes, Journal of Power Sources. 344 (2017) 15–24. https://doi.org/10.1016/j.jpowsour.2017.01.099.

[30] J. Castro-Gutiérrez, N. Díez, M. Sevilla, M.T. Izquierdo, J. Ghanbaja, A. Celzard, V. Fierro, High-Rate Capability of Supercapacitors Based on Tannin-Derived Ordered Mesoporous Carbons, ACS Sustainable Chem. Eng. 7 (2019) 17627–17635. https://doi.org/10.1021/acssuschemeng.9b03407.

[31] J.-G. Li, Y.-F. Ho, M.M.M. Ahmed, H.-C. Liang, S.-W. Kuo, Mesoporous Carbons Templated by PEO-PCL Block Copolymers as Electrode Materials for Supercapacitors, Chemistry - A European Journal. 25 (2019) 10456–10463. https://doi.org/10.1002/chem.201901724.

[50] A. Sanchez-Sanchez, M.T. Izquierdo, G. Medjahdi, J. Ghanbaja, A. Celzard, V. Fierro, Ordered mesoporous carbons obtained by soft-templating of tannin in mild conditions, Microporous and Mesoporous Materials. 270 (2018) 127–139. https://doi.org/10.1016/j.micromeso.2018.05.017.

[51] A. Elmouwahidi, J. Castelo-Quibén, J.F. Vivo-Vilches, A.F. Pérez-Cadenas, F.J. Maldonado-Hódar, F. Carrasco-Marín, Activated carbons from agricultural waste solvothermally doped with sulphur as electrodes for supercapacitors, Chemical Engineering Journal. 334 (2018) 1835–1841. https://doi.org/10.1016/j.cej.2017.11.141.

[52] Z. Li, L. Zhang, B.S. Amirkhiz, X. Tan, Z. Xu, H. Wang, B.C. Olsen, C.M.B. Holt, D. Mitlin, Carbonized Chicken Eggshell Membranes with 3D Architectures as High-Performance Electrode Materials for Supercapacitors, Advanced Energy Materials. 2 (2012) 431–437. https://doi.org/10.1002/aenm.201100548.

[53] V. Ruiz, C. Blanco, R. Santamaría, J.M. Ramos-Fernández, M. Martínez-Escandell, A. Sepúlveda-Escribano, F. Rodríguez-Reinoso, An activated carbon monolith as an electrode material for supercapacitors, Carbon. 47 (2009) 195–200. https://doi.org/10.1016/j.carbon.2008.09.048.

[54] Q. Li, R. Jiang, Y. Dou, Z. Wu, T. Huang, D. Feng, J. Yang, A. Yu, D. Zhao, Synthesis of mesoporous carbon spheres with a hierarchical pore structure for the electrochemical double-layer capacitor, Carbon. 49 (2011) 1248–1257. https://doi.org/10.1016/j.carbon.2010.11.043.

[55] A.B. Fuertes, G. Lota, T.A. Centeno, E. Frackowiak, Templated mesoporous carbons for supercapacitor application, Electrochimica Acta. 50 (2005) 2799–2805. https://doi.org/10.1016/j.electacta.2004.11.027.

[56] R. Ruiz-Rosas, M.J. Valero-Romero, D. Salinas-Torres, J. Rodríguez-Mirasol, T. Cordero, E. Morallón, D. Cazorla-Amorós, Electrochemical Performance of Hierarchical Porous Carbon Materials Obtained from the Infiltration of Lignin into Zeolite Templates, ChemSusChem. 7 (2014) 1458–1467. https://doi.org/10.1002/cssc.201301408.

[57] G.A. Ferrero, A.B. Fuertes, M. Sevilla, N-doped porous carbon capsules with tunable porosity for high-performance supercapacitors, Journal of Materials Chemistry A. 3 (2015) 2914–2923. https://doi.org/10.1039/C4TA06022A.

[58] M. Sevilla, A.B. Fuertes, A Green Approach to High-Performance Supercapacitor Electrodes: The Chemical Activation of Hydrochar with Potassium Bicarbonate, ChemSusChem. 9 (2016) 1880–1888. https://doi.org/10.1002/cssc.201600426.

[59] G. Lota, T.A. Centeno, E. Frackowiak, F. Stoeckli, Improvement of the structural and chemical properties of a commercial activated carbon for its application in electrochemical capacitors, Electrochimica Acta. 53 (2008) 2210–2216. https://doi.org/10.1016/j.electacta.2007.09.028.

[60] D.N. Futaba, K. Hata, T. Yamada, T. Hiraoka, Y. Hayamizu, Y. Kakudate, O. Tanaike, H. Hatori, M. Yumura, S. Iijima, Shape-engineerable and highly densely packed single-walled carbon nanotubes and their application as super-capacitor electrodes, Nature Materials. 5 (2006) 987–994. https://doi.org/10.1038/nmat1782.

[61] Z. Chen, J. Wen, C. Yan, L. Rice, H. Sohn, M. Shen, M. Cai, B. Dunn, Y. Lu, High-Performance Supercapacitors Based on Hierarchically Porous Graphite Particles, Advanced Energy Materials. 1 (2011) 551–556. https://doi.org/10.1002/aenm.201100114.

[62] T.E. Rufford, D. Hulicova-Jurcakova, E. Fiset, Z. Zhu, G.Q. Lu, Double-layer capacitance of waste coffee ground activated carbons in an organic electrolyte, Electrochemistry Communications. 11 (2009) 974–977. https://doi.org/10.1016/j.elecom.2009.02.038.

[63] B. Xu, F. Wu, D. Mu, L. Dai, G. Cao, H. Zhang, S. Chen, Y. Yang, Activated carbon prepared from PVDC by NaOH activation as electrode materials for high performance EDLCs with non-aqueous electrolyte, International Journal of Hydrogen Energy. 35 (2010) 632–637. https://doi.org/10.1016/j.ijhydene.2009.10.110.

[64] M. Sevilla, A.B. Fuertes, Direct Synthesis of Highly Porous Interconnected Carbon Nanosheets and Their Application as High-Performance Supercapacitors, ACS Nano. 8 (2014) 5069–5078. https://doi.org/10.1021/nn501124h.

[65] S. Gadipelli, C.A. Howard, J. Guo, N.T. Skipper, H. Zhang, P.R. Shearing, D.J.L. Brett, Superior Multifunctional Activity of Nanoporous Carbons with Widely Tunable Porosity: Enhanced Storage Capacities for Carbon-Dioxide, Hydrogen, Water, and Electric Charge, Adv. Energy Mater. 10 (2020) 1903649. https://doi.org/10.1002/aenm.201903649.

[66] L. Zhang, F. Zhang, X. Yang, G. Long, Y. Wu, T. Zhang, K. Leng, Y. Huang, Y. Ma, A. Yu, Y. Chen, Porous 3D graphene-based bulk materials with exceptional high surface area and excellent conductivity for supercapacitors, Sci Rep. 3 (2013) 1408. https://doi.org/10.1038/srep01408.

[67] Y. Zhu, S. Murali, M.D. Stoller, K.J. Ganesh, W. Cai, P.J. Ferreira, A. Pirkle, R.M. Wallace, K.A. Cychosz, M. Thommes, D. Su, E.A. Stach, R.S. Ruoff, Carbon-Based Supercapacitors Produced by Activation of Graphene, Science. 332 (2011) 1537–1541. https://doi.org/10.1126/science.1200770.

[68] L. Wei, M. Sevilla, A.B. Fuertes, R. Mokaya, G. Yushin, Hydrothermal Carbonization of Abundant Renewable Natural Organic Chemicals for High-Performance Supercapacitor Electrodes, Advanced Energy Materials. 1 (2011) 356–361. https://doi.org/10.1002/aenm.201100019.